geosciences

MDPI

Article

Parametric Controls on Dynamic CO_2 Storage Capacity in a Saline Aquifer: The Lopín Structure Case Study (Ebro Basin, NE Spain)

Camilo Antonio Quintero-Tejada [1], Ignasi Herms [2,*], Marc Gil-Ortiz [1,3], Jesús García-Crespo [4] and Paula Fernández-Canteli [4]

[1] Màster d'Energies Renovables i Sostenibilitat Energètica, Facultat de Física, Universitat de Barcelona (UB), 08028 Barcelona, Spain; camiloquintej@gmail.com (C.A.Q.-T.); marc.gilortiz@ub.edu (M.G.-O.)
[2] Àrea de Recursos Geològics, Institut Cartogràfic i Geològic de Catalunya (ICGC), 08038 Barcelona, Spain
[3] Departament de Dinàmica de la Terra i de l'Oceà, Facultat de Ciències de la Terra, Universitat de Barcelona (UB), c/Martí i Franquès s/n, 08028 Barcelona, Spain
[4] Grupo Geoenergía, Instituto Geológico y Minero de España (IGME-CSIC), 28003 Madrid, Spain; garcia.crespo@igme.es (J.G.-C.); paula.canteli@igme.es (P.F.-C.)
* Correspondence: ignasi.herms@icgc.cat

Abstract

Pressure-limited dynamic capacity in the Lopín structure is controlled primarily by reservoir transmissibility rather than by static pore volume. This study applies a MATLAB/MRST vertical-equilibrium (VE) workflow to the Lopín horst, a deep Triassic Buntsandstein aquifer in the Ebro Basin, NE Spain, and evaluates the sensitivity of the results to seven petrophysical, fluid, and operational parameters using a one-at-a-time sensitivity design (35 sensitivity cases plus one base case). Across the tested range, horizontal permeability produced the largest variation in maximum injectable CO_2 mass, from 4.67 to 16.25 Mt (range 11.59 Mt), followed by the adopted BHP threshold (range 5.33 Mt) and CO_2 density (range 4.74 Mt). Porosity and brine compressibility had only minor effects, whereas injection rate and residual CO_2 saturation did not change the BHP-limited capacity under the adopted capacity-search formulation. The base-case operational BHP limit was 28.5 MPa, selected below the site-specific allowable- and estimated fracture-pressure thresholds reported for Lopín. These results show that pressure dissipation, hydraulic transmissibility, and the explicit choice of operational pressure criterion are the dominant controls on dynamic CO_2 storage capacity in this fault-bounded saline aquifer.

Keywords: geological CO_2 storage; dynamic storage capacity; bottom-hole pressure; vertical equilibrium; MRST; Lopín horst

Check for updates

Academic Editor: Massimo Zecchin

Received: 11 September 2026
Revised: 3 October 2026
Accepted: 8 October 2026
Published: 11 October 2026

Copyright: © 2026 by the authors. Licensee MDPI, Basel, Switzerland. This article is an open access article distributed under the terms and conditions of the Creative Commons Attribution (CC BY) license.

1. Introduction

Geological storage of CO_2 is widely recognized as a key component of carbon capture and storage (CCS) strategies for reducing emissions from industrial sectors that are difficult to decarbonize through electrification alone [1,2]. Among the available geological options, deep saline aquifers are particularly relevant because of their broad distribution in sedimentary basins and their high theoretical storage potential [1,3,4]. However, these systems present specific technical challenges, including limited prior subsurface information, buoyancy-driven CO_2 migration, brine displacement, lower storage efficiency than depleted hydrocarbon reservoirs, and pressure build-up during injection [3,4]. Therefore, reliable assessment of saline aquifer storage sites requires not only estimating available pore

volume, but also dynamically analyzing pressure evolution, injectivity, plume migration, and long-term containment.

The concept of CO_2 storage capacity has evolved from static volumetric estimation toward dynamic, pressure-constrained assessments. Static methods commonly estimate capacity as a fraction of the available pore volume using storage-efficiency coefficients [5]. These approaches are useful for regional screening, but they do not fully capture the hydraulic response of the reservoir during injection. Several studies have shown that pressure build-up may become a primary limitation on the effective capacity of deep saline aquifers, especially in closed or semi-closed systems where displaced brine cannot dissipate freely [6–9]. In such cases, the technically achievable capacity may be significantly lower than the theoretical volumetric capacity, and the maximum injectable mass is controlled by reservoir transmissibility, boundary conditions, well configuration, injection strategy, and admissible pressure thresholds.

Pressure management is closely linked to storage safety. Quick pressure increases may sometimes compromise seal integrity, induce hydraulic fracturing, reactivate faults, or generate leakage pathways through pre-existing discontinuities [6,7,10]. For this reason, operational storage assessments commonly incorporate bottom-hole pressure (BHP) limits or other admissible pressure criteria as practical constraints on injection. These thresholds establish a link between multiphase-flow simulation and geomechanical safety, even when fully coupled hydro-mechanical modeling is not yet available. Consequently, pressure-limited dynamic capacity should be reported together with the adopted pressure criterion and its geological or geomechanical justification.

In this sense, numerical simulation provides the most appropriate framework for evaluating pressure-limited dynamic capacity because it can represent the coupled effects of multiphase flow, buoyancy, pressure propagation, fluid properties, and operational constraints. Three-dimensional models can capture geological heterogeneity in detail, but their computational cost increases considerably when long-term post-injection behavior, uncertainty, or multiple sensitivity scenarios must be analyzed. Vertical-equilibrium (VE) models offer an efficient alternative for laterally extensive saline aquifers, where vertical segregation of CO_2 by buoyancy occurs faster than large-scale lateral migration [11,12]. In VE formulations, the three-dimensional problem is reduced to a vertically integrated representation that preserves the dominant physics of buoyancy-driven migration, pressure dissipation, and regional plume evolution.

The MATLAB Reservoir Simulation Toolbox (MRST) [13,14] and its co2lab module [SINTEF] have played an important role in developing open-source workflows for geological CO_2 storage modeling. MRST-co2lab includes tools for structural trapping analysis, spill-point identification, VE simulation, long-term migration assessment, and basin-scale capacity estimation [12–17]. Previous MRST/co2lab studies have demonstrated the value of vertically integrated models for estimating trapping capacity, optimizing aquifer-wide storage, and simulating large-scale CO_2 migration over long time scales [14–18]. Recent work has also demonstrated three-dimensional geological CO_2 sequestration simulations using MRST [19], while other studies have expanded the use of VE and reduced-complexity models to evaluate storage efficiency, well placement, and computationally efficient sensitivity workflows [20–22]. These advances show that VE and MRST-based approaches are well established; however, their application to real cases of fault-bounded saline aquifers, considering site-specific pressure limits and systematic BHP-constrained capacity ranking, remains poorly studied.

In Spain, CO_2 storage research has advanced through national screening initiatives, site-specific characterization studies, and European collaborative projects. The ALGECO2 initiative provided an early framework for identifying suitable structures for geological storage. Subsequent studies focused on the Hontomín experimental plant and on the petrographic, hydraulic, geological, and geochemical characterization of potential reservoirs and seals [23–27]. In the Ebro Basin, recent work has highlighted the potential of several structures and has applied integrated geological and geophysical methodologies to the Lopín structure [28]. European-funded projects including STRATEGY CCUS, PilotSTRATEGY, and GSEU have further reinforced interest in deep saline aquifers as a strategic resource for regional decarbonization [29–35].

Despite these advances, a specific gap of knowledge remains at the intersection of pressure-limited dynamic capacity and fault-bounded saline aquifers. Previous studies have provided important advances in static capacity estimation, pressure-constrained capacity theory, VE model development, MRST/co2lab workflows, and characterization of Spanish storage sites [5–35]. However, few published studies combine: (i) a real ECLIPSE/GRDECL geocellular model, where GRDECL refers to the grid and property-deck format commonly used by reservoir simulators, of onshore saline aquifers in Spain; (ii) a VE workflow adapted to a fault-bounded horst structure; (iii) mixed hydraulic boundary conditions representing partial lateral connection with the regional aquifer; and (iv) a systematic one-at-a-time ranking of BHP-limited dynamic capacity.

The Lopín structure, located in the southern sector of the Ebro Basin (Spain), provides a suitable case study to address this gap. The target reservoir, confined by low-permeability sealing units and bounded by normal faults, makes this structural configuration in Lopín particularly relevant for analyzing how permeability, lateral pressure dissipation, hydraulic boundary conditions, and operational pressure limits control dynamic storage capacity. In this context, the present study develops and applies a MATLAB/MRST VE workflow to quantify the parametric controls on pressure-limited CO_2 storage capacity in the Lopín structure.

The central hypothesis of this work is that, in fault-bounded saline aquifers such as Lopín, operational CO_2 storage capacity is governed more strongly by pressure dissipation and hydraulic transmissibility than by static pore volume alone. To test this hypothesis, the study uses a probabilistic realization with two injection wells, mixed hydraulic boundary conditions, and a BHP-constrained capacity-search algorithm over a 30-year injection period. A one-at-a-time sensitivity analysis is then performed on seven parameter groups: porosity, horizontal permeability, injection rate, BHP limit, brine compressibility, residual CO_2 saturation, and CO_2 density. By identifying the parameters that most strongly control dynamic capacity, this work aims to support early-stage site characterization, pilot design, and preliminary safety assessment of structurally compartmentalized saline aquifers.

2. Geological Setting

The Lopín structure is located in the southern sector of the Ebro Basin, northeastern Spain (Figures 1 and 2). The Ebro Basin is one of the major sedimentary basins of the Iberian Peninsula and contains several deep geological formations that have been evaluated for subsurface energy applications and CO_2 storage [26–30]. Within this setting, Lopín is an onshore, fault-bounded structural high selected as a candidate site within the H2020 PilotSTRATEGY project for geological CO_2 storage [29,30].

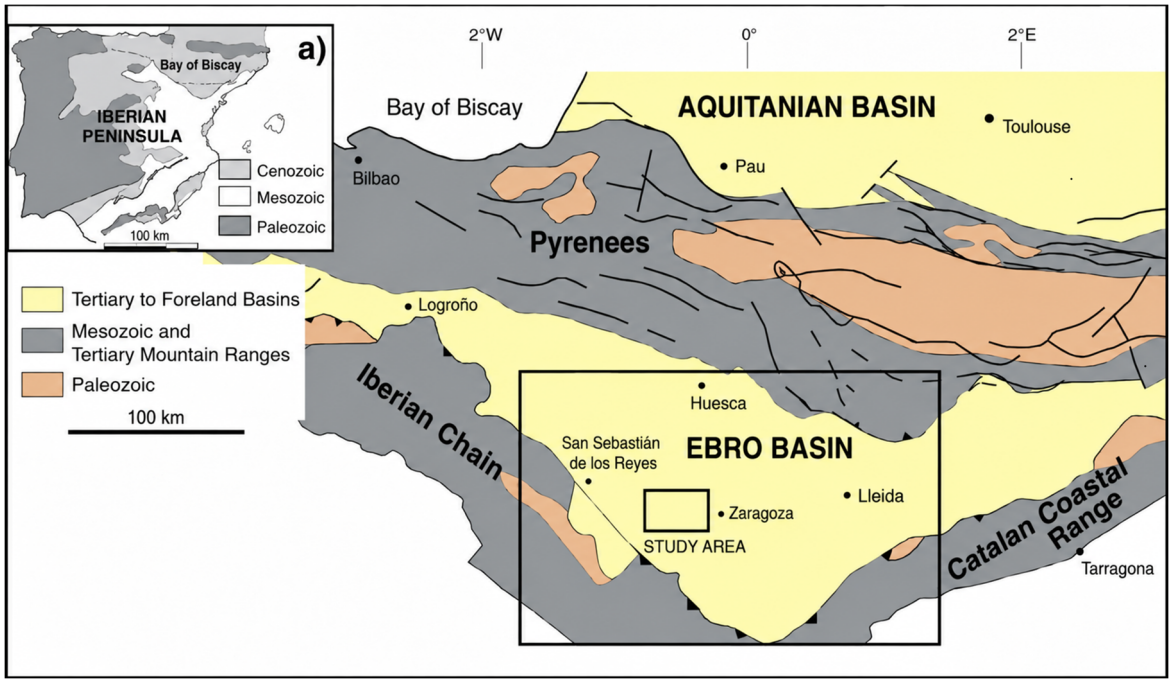


Figure 1. Regional setting of the Ebro Basin in northeastern Spain. (a) Simplified geological map of the Iberian Peninsula.

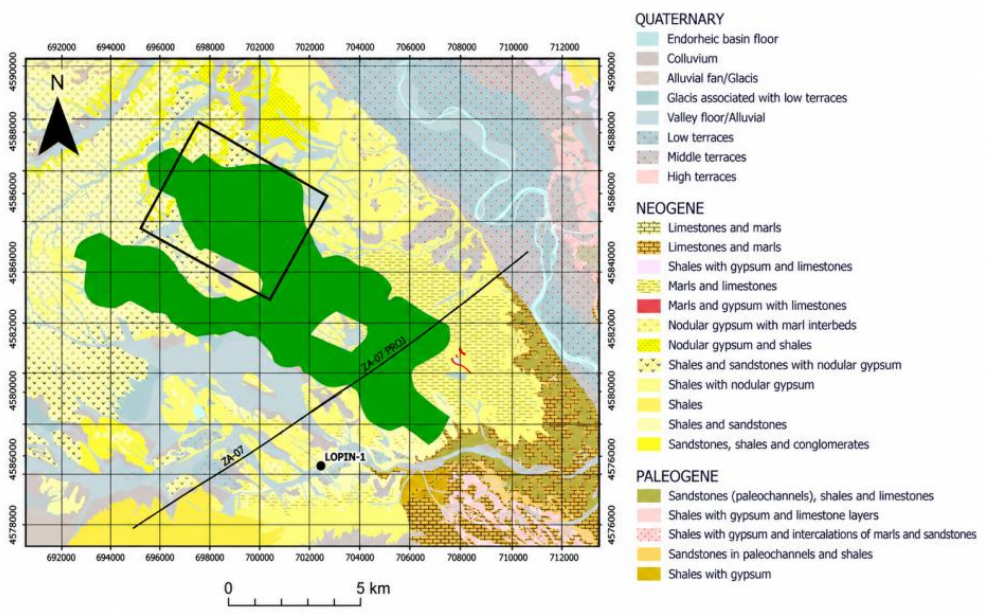


Figure 2. Geological map of the Lopín area showing the interpreted structural closure of the storage structure and the simulation-grid domain used in the numerical model. The green shaded area in the panel represents the structural closure/modeled domain, not a lithological unit.

Structurally, Lopín is interpreted as an NW-SE-trending horst bounded by normal faults (Figure 3). The main target reservoir is the Triassic Buntsandstein B1 unit, a sandstone formation located at approximately 1760 m depth. The reservoir is overlain by low-permeability Triassic clay-rich and evaporitic units that constitute the main sealing interval. The fault-bounded geometry is relevant for storage assessment because it may control both hydraulic compartmentalization and lateral pressure dissipation [28–30].

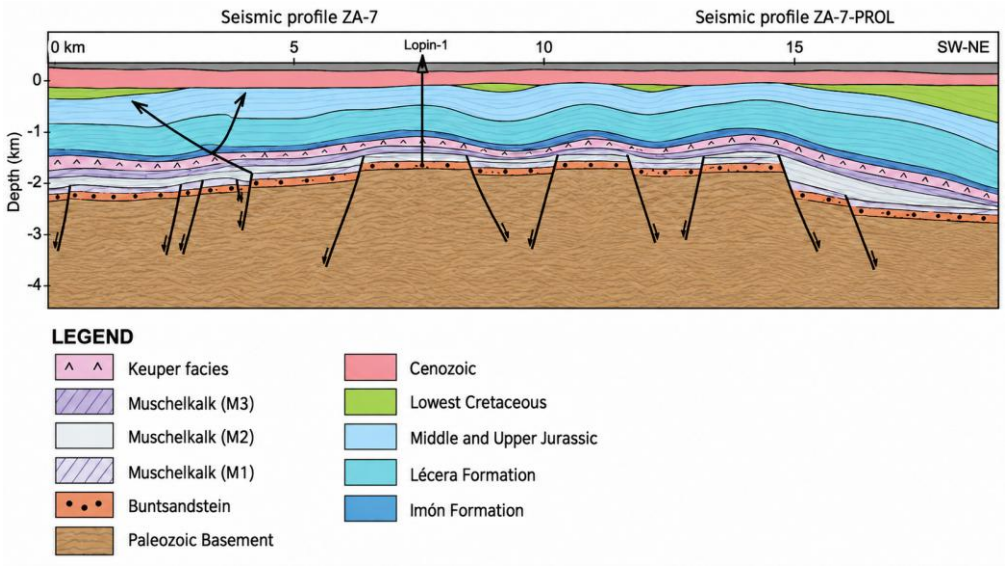


Figure 3. Interpreted geological cross-section along seismic profiles ZA-7 and ZA-7-PROL, showing the main stratigraphic units, basement structure, normal faults, and the position of the Lopin-1 well. Panels adapted from the PilotSTRATEGY geological characterization [29,30].

3. Dataset and Methods

3.1. Dataset

The geological and petrophysical data used in this study were provided by IGME-CSIC within the PilotSTRATEGY project in ECLIPSE/GRDECL format [29,30]. The files included the three-dimensional reservoir geometry, porosity distribution, horizontal permeability fields, geological units, shale volume, active-cell mask, and fault traces.

The original geocellular model contains 160,532 active cells. From this model, a VE representation was generated with 2820 columns, of which 2808 were active for simulation. The P10, P50, and P90 probabilistic realizations were supplied by IGME-CSIC as pre-built ECLIPSE/GRDECL models generated within the upstream PilotSTRATEGY geological-modeling workflow; their generation and calibration were not performed as part of this study. Accordingly, the present work treats them as externally provided geological uncertainty realizations. The P50 realization was selected as the reference case because it represents the central condition of the available dataset, whereas P10 and P90 define the broader uncertainty context.

The pressure-limited dynamic capacity, hereafter CapBHP, is defined as the maximum injectable CO_2 mass over 30 years that does not exceed the adopted BHP limit.

3.2. Methodology

3.2.1. Modeling Approach

CO_2 injection and migration were simulated using a VE approach in MATLAB R2025b/MRST. The formulation assumes that buoyant CO_2 segregates rapidly toward the top of the reservoir compared with large-scale lateral migration. Under these conditions, each vertical reservoir column can be represented through integrated variables, allowing the model to capture reservoir-scale pressure evolution and plume migration at a lower computational cost than a full three-dimensional multiphase model.

The main dynamic variables were pore pressure and accumulated CO_2 height in each column. From these variables, equivalent CO_2 saturation, plume extent, pressure evolution, and trapping indicators were estimated during the injection and post-injection periods. MRST/co2lab served as a conceptual and computational reference, but the workflow was adapted to the Lopín geometry to directly control the vertical integration of the original 3D

geocellular grid into VE columns, the mixed boundary conditions, the well configuration, and the iterative BHP-limited capacity search.

The numerical workflow followed five main stages: (1) input-data preparation, (2) conversion from the 3D grid to the VE grid, (3) application of the MRST's fully implicit Newton-AD solver to calculate the pressure and CO_2-height variables, (4) BHP-based injection control, and (5) post-processing of plume geometry, pressure evolution, dynamic capacity, trapping inventory, and mass balance (Figure 4).

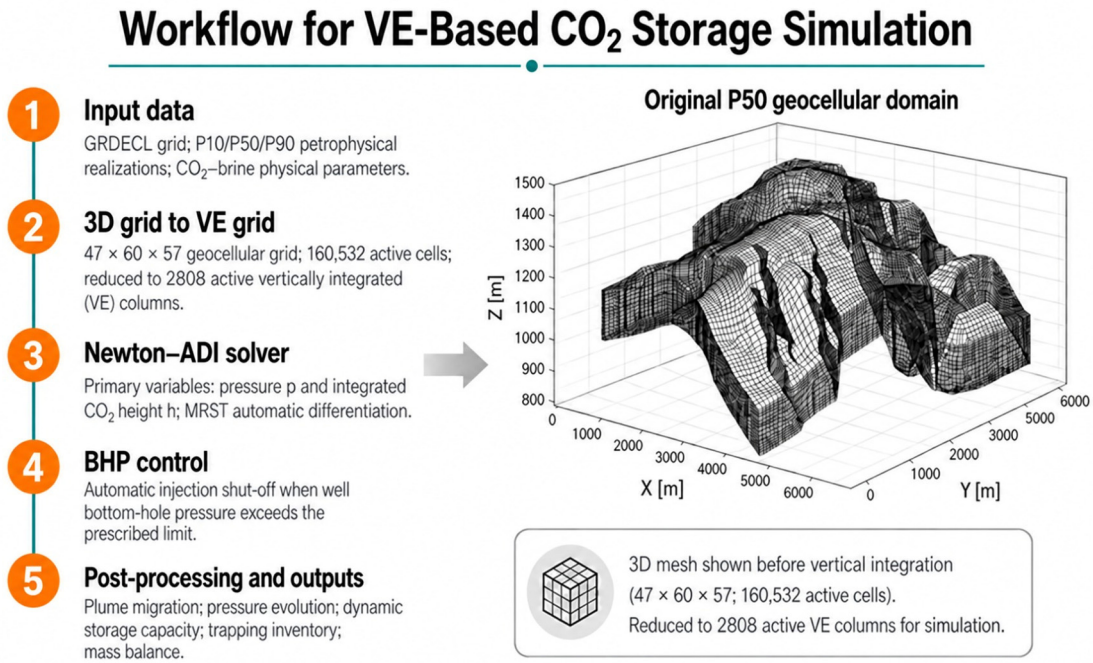


Figure 4. Workflow used to estimate the dynamic CO_2 storage capacity of the Lopín structure. The 3D mesh shown on the right represents the original P50 geocellular domain (47 × 60 × 57; 160,532 active cells) before reduction to 2808 active VE columns. The workflow then applies the VE solution, BHP-based injection control, and post-processing of plume migration, pressure, capacity, trapping inventory, and mass balance.

3.2.2. Boundary Conditions, Wells, and Capacity Criterion

The geological configuration of the Lopín horst was represented in the numerical model using mixed hydraulic boundary conditions to simulate a partially open system. The northern and southern boundaries, corresponding to the main faults that structurally bound the horst, were defined as no-flow boundaries. In contrast, the eastern and western boundaries were assigned hydrostatic pressure conditions to represent lateral hydraulic connection with the regional aquifer. This configuration represents an intermediate hydraulic behavior between a closed structural compartment and a fully open saline aquifer.

Injection was simulated through two active wells, C1 and C2. C1 is located on the northwestern flank and C2 near the structural crest (Figure 5); therefore, this pair was selected as the reference configuration to distribute injection and reduce local pressure build-up. Three injection-related quantities are distinguished in this study. First, the P50 reference rate reported in the PilotSTRATEGY safety and performance assessment for Lopín [30] is 0.254 Mt/year, corresponding to 7.62 Mt over 30 years, and is used here only as an external comparison. Second, the long-term P50 plume-migration simulation injects 8.46 Mt over 30 years, corresponding to an average total rate of 0.282 Mt/year distributed between the two active wells. Third, the BHP-limited capacity-search algorithm estimates the maximum admissible injected mass over the same 30-year period without exceeding

the selected BHP criterion. The complete set of base-case parameters is summarized in Table 1.

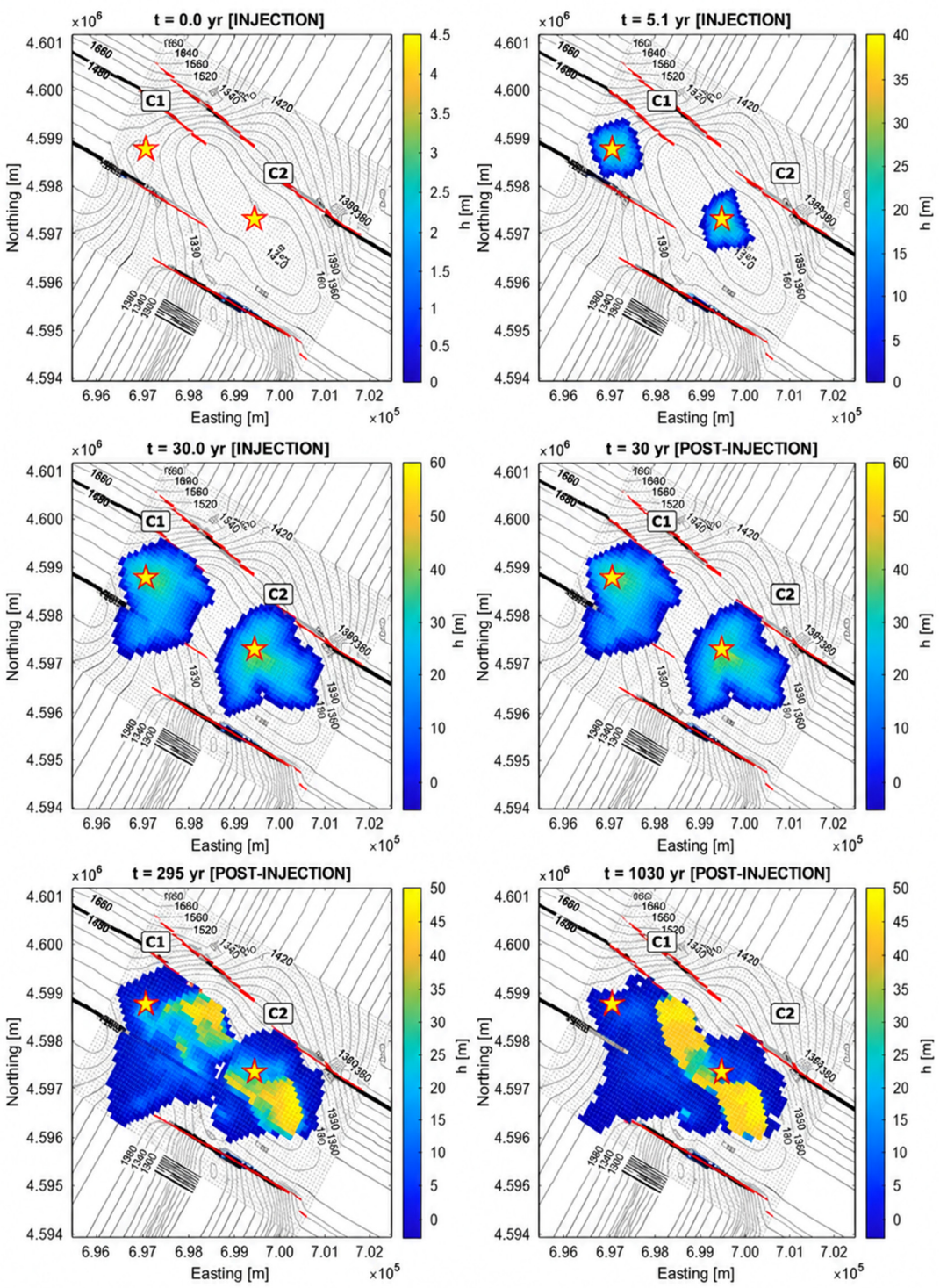


Figure 5. Spatial evolution of integrated CO_2 plume height in the P50 reference scenario, arranged as a 2-column × 3-row sequence for improved readability. Panels show t = 0, 5.1, and 30 years during injection, followed by t = 30, 295, and 1030 years during post-injection. Stars indicate the C1 and C2 injection wells; colored cells represent integrated CO_2 height h; and contours show reservoir-top depth and the structural framework controlling migration.

Table 1. Main parameters of the P50 base case.

Parameter	Base Value	Unit	Function in the Model	Source
Reference depth	1760	m	Defines the initial reservoir state	PilotSTRATEGY geological model [29,30]
Reference pressure	21.5	MPa	Basis of the hydrostatic pressure field	Site-specific hydrostatic reference pressure [30]
Brine density	1120	kg/m^3	Controls hydrostatic pressure and buoyancy	Site-specific fluid parameter/model assumption
CO_2 density	700	kg/m^3	Controls density contrast	Base-case constant-density assumption
Brine viscosity	8×10^{-4}	Pa·s	Controls aqueous-phase mobility	Constant base-case fluid-property assumption used in the MATLAB/MRST VE model
CO_2 viscosity	6×10^{-5}	Pa·s	Controls CO_2 mobility	Constant base-case fluid-property assumption used in the MATLAB/MRST VE model
Brine compressibility	4.0×10^{-10}	Pa^{-1}	Influences pressure propagation	Base-case compressibility value used in the pressure equation; evaluated in the sensitivity analysis
Irreducible water saturation	0.20	—	Reduces pore space available for CO_2	Base-case saturation parameter used to define effective pore volume available for CO_2
Residual CO_2 saturation	0.18	—	Controls residual-trapping diagnosis	Base-case residual-trapping parameter; evaluated in the sensitivity analysis
Mean porosity, P50	9.32	%	Base petrophysical property	P50 GRDECL realization [29,30]
Arithmetic-mean horizontal permeability, P50	14.95	mD	Main control on transmissibility	P50 GRDECL realization [29,30]
Nominal injection rate	0.254	Mt/year	Base injection rate for the P50 scenario	P50 reference operational rate used in the Lopín base-case simulation
BHP limit	28.5	MPa	Main capacity criterion	Conservative operational threshold below p90, pAllow, and pFrac [30]

Dynamic storage capacity was defined as the maximum mass of CO_2 that can be injected over the 30-year period without exceeding the selected operational BHP criterion (28.5 MPa). This definition distinguishes pressure-constrained dynamic capacity from

static pore-volume capacity and explicitly links the capacity estimate to an operational pressure constraint. The BHP-limited capacity search was performed in two stages. First, a logarithmic scan of candidate injected masses was used to identify the transition between pressure-safe and pressure-exceeding cases. Second, a binary search was applied within this interval to refine the maximum admissible mass. For each candidate mass, the corresponding total injection rate was obtained by dividing the mass by the fixed 30-year injection period and was distributed equally between the active wells. A candidate mass was accepted only if the maximum BHP reached at any active well and at any time step during injection remained below the prescribed BHP limit. Cap_BHP is therefore the largest accepted mass satisfying this criterion.

The reference BHP limit was set to 28.5 MPa as a conservative operational constraint within the site-specific geomechanical pressure envelope reported for Lopín [30]. This threshold is 1.1 MPa below the P90 scenario (P90 = 29.6 MPa), 2.0 MPa below the allowable pressure (pAllow = 30.5 MPa), and 4.4 MPa below the estimated fracture pressure (pFrac = 32.9 Mpa). The 28.5 MPa value is therefore not interpreted as the fracture pressure itself, but as a modeling threshold that preserves a pressure buffer to the upper geomechanical limits. The sensitivity analysis subsequently varies this operational threshold from 26.31 to 30.50 MPa to quantify how the selected pressure criterion affects dynamic capacity. The reference pressure evolution is contextualized against the site-specific p80, p90, pAllow, and pFrac levels in Figure 6; these contextual lines do not control the capacity-search algorithm. Therefore, the injection was not stopped at 28.5 MPa because this value represents the fracture pressure, but because it was adopted as a conservative operational BHP threshold that preserves a pressure buffer below the upper geomechanical limits.

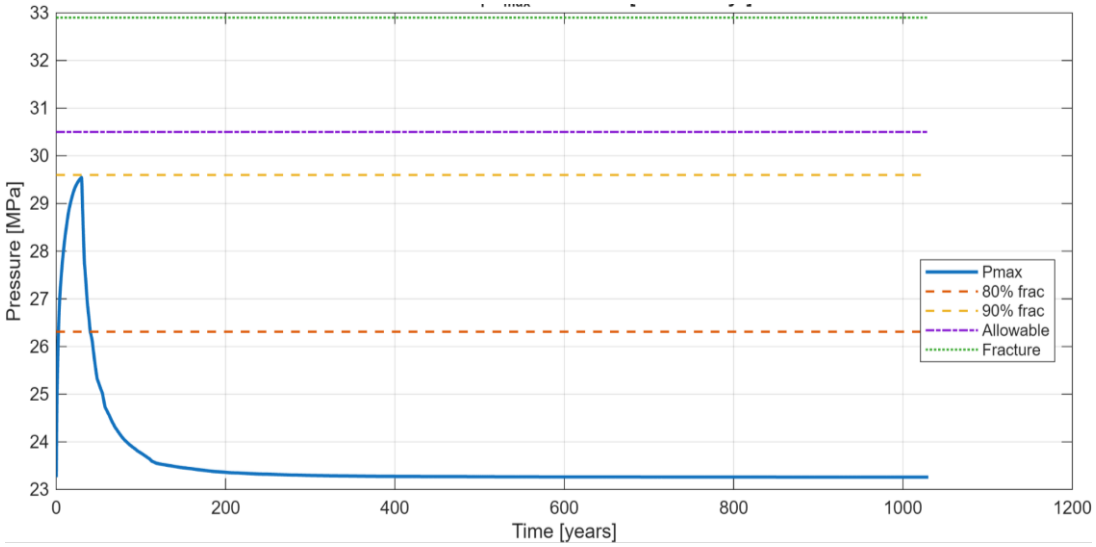


Figure 6. Temporal evolution of maximum reservoir pressure for the P50 reference simulation with two active wells and mixed boundary conditions. The horizontal lines show the site-specific p80 = 26.31 MPa, p90 = 29.60 MPa, pAllow = 30.50 MPa, and pFrac = 32.90 MPa reference levels [30]. The operational BHP criterion used by the capacity-search algorithm is evaluated at the injection wells and is discussed separately in Section 3.2.2.

3.2.3. Sensitivity Analysis Design

The central objective of the sensitivity analysis was to identify which parameters exert the strongest control on pressure-limited dynamic storage capacity. For this purpose, a one-at-a-time (OAT) analysis was applied, in which one parameter is modified while all others remain at their base-case values to evaluate the real impact of the variation in this parameter over the modeling.

Seven parameter groups were evaluated: porosity, permeability, injection rate, BHP limit, brine compressibility, residual CO_2 saturation, and CO_2 density. Each parameter group was evaluated using five prescribed parameter values, resulting in 35 sensitivity simulations plus one base case, for a total of 36 simulations. The tested parameters and base values are summarized in Table 2. The system response was evaluated using two indicators: pressure-limited dynamic capacity, expressed in Mt CO_2, and maximum pressure reached during the simulation, expressed in MPa.

Table 2. One-at-a-time (OAT) sensitivity analysis design.

Group	Evaluated Parameter	Tested Values	Base Value
G1	Porosity multiplier	×0.70; ×0.85; ×1.00; ×1.15; ×1.30	×1.00
G2	Permeability multiplier	×0.25; ×0.50; ×1.00; ×2.00; ×4.00	×1.00
G3	Injection rate	0.15; 0.20; 0.254; 0.32; 0.40 Mt/year	0.254 Mt/year
G4	BHP limit	26.31; 27.50; 28.50; 29.50; 30.50 MPa	28.50 MPa
G5	Brine compressibility	×0.50; ×0.75; ×1.00; ×1.50; ×2.00	×1.00
G6	Residual CO_2 saturation	0.08; 0.13; 0.18; 0.23; 0.28	0.18
G7	CO_2 density	550; 625; 700; 775; 850 kg/m^3	700 kg/m^3

The porosity and permeability multipliers were applied to the P50 realization as controlled parametric perturbations. They should not be interpreted as direct percentiles of the original geostatistical distributions because the P10, P50, and P90 models were supplied as pre-built geological realizations by IGME-CSIC, and their full underlying property distributions were not recalibrated in this study. Instead, the multipliers were used to test how uniform changes in pore volume and horizontal transmissibility affect pressure-limited capacity around the P50 reference model. The P10 and P90 realizations therefore provide the broader geological uncertainty context, whereas the multiplier analysis provides a local sensitivity test around P50.

Fluid properties were treated as constant modeling parameters in the present VE workflow. The base-case CO_2 density of 700 kg/m^3 was adopted as a representative dense-phase value for the Lopín reservoir-depth conditions, with the Buntsandstein B1 reservoir located at approximately 1760 m depth. Because no well-specific PVT measurements or direct reservoir-fluid samples were available, CO_2 density was not computed from a pressure-, temperature-, and salinity-dependent equation of state. Instead, the 550–850 kg/m^3 range was used as a parametric uncertainty interval to evaluate the influence of representative dense-phase property uncertainty on pressure-limited dynamic capacity. Salinity was not explicitly coupled to the density calculation; it was only represented in the dissolution diagnostic through a maximum dissolution of 2%, consistent with highly saline brine conditions of the order of 150,000 ppm NaCl. Therefore, the density cases should be interpreted as parametric sensitivity scenarios rather than thermodynamic end members.

4. Results

The results presented in this section correspond to the P50 reference case, using the C1–C2 well configuration and mixed hydraulic boundary conditions described in Section 3.2.2. This configuration was kept fixed throughout the sensitivity analysis to

isolate the influence of petrophysical, fluid, and operational parameters on pressure-limited dynamic capacity.

Three related but distinct quantities are reported. First, the P50 reference value reported in the PilotSTRATEGY safety and performance assessment for Lopín [30] corresponds to 7.62 Mt over 30 years, derived from a reference rate of 0.254 Mt/year, and is used here only as an external comparison. Second, the long-term P50 plume-migration simulation injects 8.46 Mt of CO_2 over 30 years and evaluates pressure evolution, plume migration, and trapping behavior during 1000 years of post-injection. Third, the BHP-limited capacity search estimates the maximum injectable mass over the same 30-year injection period without exceeding the adopted operational pressure limit. These quantities should therefore not be interpreted as the same result.

4.1. Pressure Evolution, Plume Migration, and Dynamic Capacity

In the long-term P50 reference simulation, approximately 8.46 Mt CO_2 is injected over 30 years. Maximum pressure increases during injection, reaches its peak near the end of the injection phase, and then decreases rapidly once injection stops. This decline reflects pressure dissipation through the hydraulically open east–west boundaries, whereas the north and south boundaries, associated with faults, restrict transverse flow.

The capacity-to-reference ratio was calculated by comparing the BHP-limited capacity obtained in this study with the P50 reference mass reported in the PilotSTRATEGY safety and performance assessment for Lopín [30]. For the P50 C1–C2 case with mixed boundary conditions, the modeled Cap_BHP is 10.71 Mt, whereas the PilotSTRATEGY reference mass is 7.62 Mt; therefore, the capacity-to-reference ratio is 10.71/7.62 = 1.41. This ratio does not refer to the long-term plume-migration simulation mass of 8.46 Mt, which remains below the pressure-limited capacity.

The maximum-pressure curve exceeds the conservative p80 threshold during injection and approaches the threshold corresponding to 90% of the fracture pressure but remains below the allowable-pressure and estimated fracture-pressure criteria. This behavior indicates that the reference configuration preserves a safety margin with respect to the upper limits, although it temporarily operates within the conservative alert zone.

Plume migration is governed by buoyancy-driven upward segregation within each VE column and lateral spreading beneath the seal (Figure 5). At early injection times, the plume develops around C1 and C2 sites as two separate accumulations. By the end of injection, both accumulations expand laterally following the structural relief of the reservoir top. During post-injection, the plume continues to redistribute, increases its lateral extent, and preferentially concentrates in structurally shallower areas.

4.2. Storage Mechanisms

The long-term reference simulation indicates that storage security evolves after the end of injection as the CO_2 plume redistributes beneath the vertical seal and is progressively partitioned among mobile, residual, structural, and dissolved fractions. During the post-injection period, part of the mobile CO_2 becomes immobilized by residual trapping as the plume migrates, while another fraction is retained in local structural closures or dissolves into the brine.

At 1030 years, the diagnostic inventory indicates that approximately 77% of the CO_2 remains mobile, 18% is residually trapped, 4% is structurally trapped, and less than 1% is dissolved (Figure 7). These results show that, for the simulated configuration, storage security depends not only on structural retention but also on the progressive evolution of residual trapping. At the same time, the high proportion of mobile CO_2 underlines the importance of evaluating long-term plume migration and seal continuity.

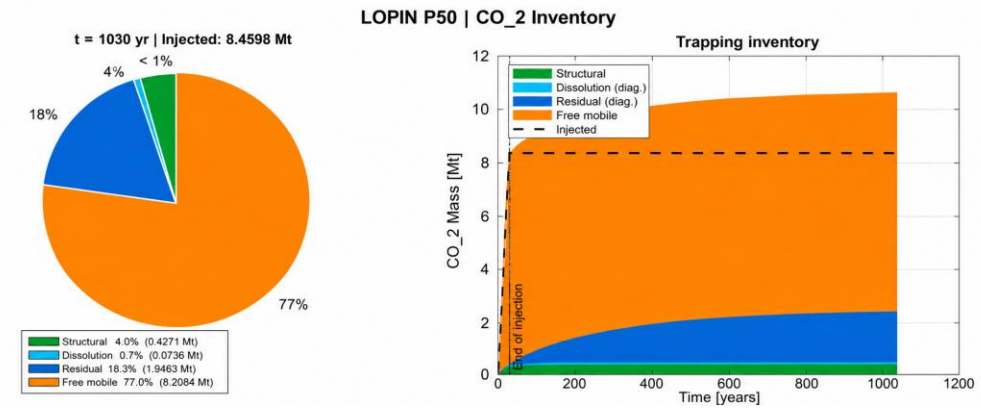


Figure 7. CO_2 trapping inventory for the P50 reference scenario. **Left**: final partitioning of CO_2 among structural, dissolved, residual, and mobile fractions after 1030 years. **Right**: temporal evolution of the trapping inventory throughout the full simulation, including cumulative injected mass.

4.3. Parametric Sensitivity Ranking of Dynamic Capacity

The P50 reference case, using the C1–C2 well configuration and mixed boundary conditions, fixed throughout the sensitivity analysis, allows the individual influence of petrophysical, fluid, and operational parameters on pressure-limited dynamic capacity to be isolated. The one-at-a-time (OAT) analysis described in Section 3.2.3 varies each parameter group independently while keeping the others at their base-case values. This ranking should be interpreted as conditional on the selected one-at-a-time parameter ranges. It does not represent a global sensitivity analysis and does not capture interactions among petrophysical, fluid, boundary-condition, and operational parameters. Therefore, the ranking identifies the dominant controls within the prescribed perturbation space, rather than universal parameter importance.

Among the seven parameter groups, horizontal permeability appears to be the dominant controlling factor. When the permeability multiplier varies between $\times 0.25$ and $\times 4.00$, Cap_BHP ranges from 4.665 to 16.252 Mt, with a total range of 11.588 Mt. This range is approximately 107.7% of the base-case capacity (Table 3; Figure 8). Here, Cap_BHP denotes the maximum injectable CO_2 mass over the 30-year injection period without exceeding the adopted BHP limit.

Table 3. Sensitivity ranking for pressure-limited dynamic capacity.

Rank	Parameter	Minimum Cap BHP [Mt]	Maximum Cap BHP [Mt]	Range [Mt]	Relative Importance
1	Horizontal permeability	4.66	16.25	11.58	107.7%
2	BHP limit	7.93	13.25	5.32	49.5%
3	CO_2 density	8.34	13.09	4.74	44.1%
4	Porosity	10.34	10.76	0.41	3.9%
5	Brine compressibility	10.59	10.92	0.33	3.1%
6	Injection rate; residual CO_2 saturation	10.76	10.76	0.00	0.0%

The second most influential parameter is the BHP limit. When the admissible pressure threshold varies between 26.31 and 30.50 MPa, capacity changes from 7.931 to 13.257 Mt, corresponding to a range of 5.326 Mt. This confirms that the operational definition of the pressure limit has a direct effect on the maximum injectable mass.

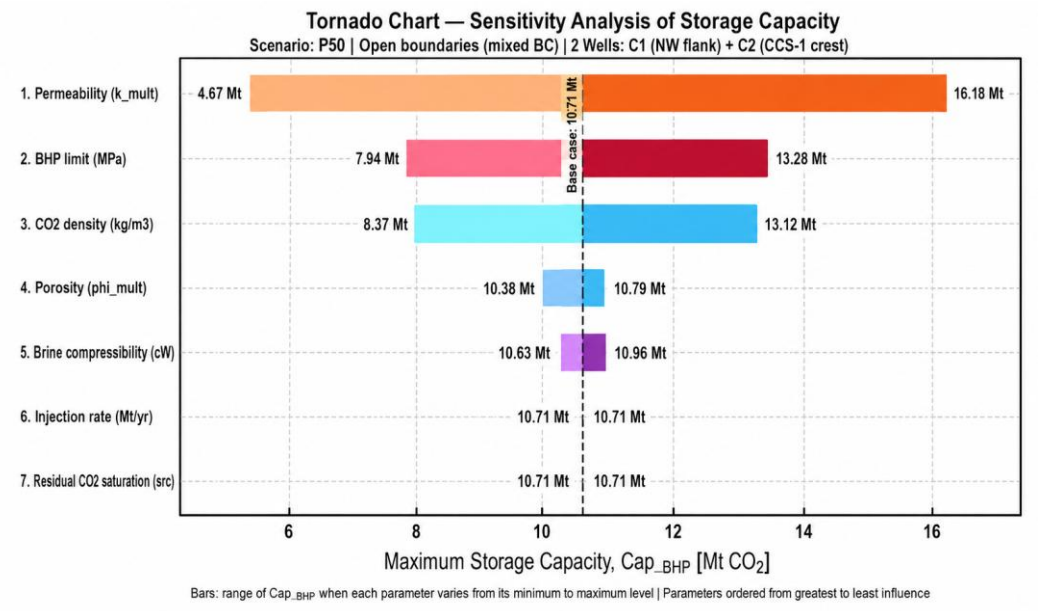


Figure 8. Tornado chart of the OAT sensitivity analysis for the P50 scenario with two wells and mixed boundary conditions. Cap_BHP denotes the maximum injectable CO_2 mass over 30 years without exceeding the adopted BHP limit. The vertical line represents the base-case capacity (Cap_BHP = 10.760 Mt), and bar length shows the capacity range associated with each parameter. Parameters are ordered from the largest to the smallest influence.

The third most influential parameter is CO_2 density. Over the evaluated range between 550 and 850 kg/m^3, capacity varies from 8.347 to 13.090 Mt, with a range of 4.743 Mt. Together, these three parameters, permeability, BHP limit, and CO_2 density, explain nearly all relevant variability in pressure-limited dynamic capacity. In contrast, porosity and brine compressibility show a much smaller influence, while injection rate and residual CO_2 saturation do not change Cap_BH under the adopted search formulation.

Permeability exhibits the strongest and most nonlinear response in terms of CO_2 storage capacity (Figure 9). When the permeability multiplier is reduced to $\times$0.25, capacity decreases to 4.66 Mt, indicating a strong limitation in lateral pressure dissipation. With a multiplier of $\times$0.50, capacity increases to 6.60 Mt but remains clearly below the base case. In contrast, doubling permeability increases capacity to 16.25 Mt, the maximum robust value obtained across the sensitivity set. The $\times$4.00 case produced an anomalous numerical response with non-finite maximum pressure. This case is therefore retained for transparency but excluded from the physical interpretation of the permeability trend. The robust upper-end response of the permeability sensitivity is represented by the $\times$2.00 case, which yielded the maximum physically interpretable capacity of 16.252 Mt.

The BHP limit acts as direct design control. When the conservative threshold of 26.31 MPa is used, maximum capacity decreases to 7.93 Mt. When the criterion is relaxed to 30.50 MPa, capacity increases to 13.25 Mt. This difference shows that the selected pressure limit can have an impact comparable to key physical properties of the storage system.

CO_2 density also significantly affects capacity. At the lowest evaluated density, 550 kg/m^3, capacity decreases to 8.34 Mt. At the highest density, 850 kg/m^3, it increases to 13.090 Mt. This response indicates that thermodynamic fluid properties influence pressure behavior and, consequently, the maximum mass that can be injected under the BHP criterion.

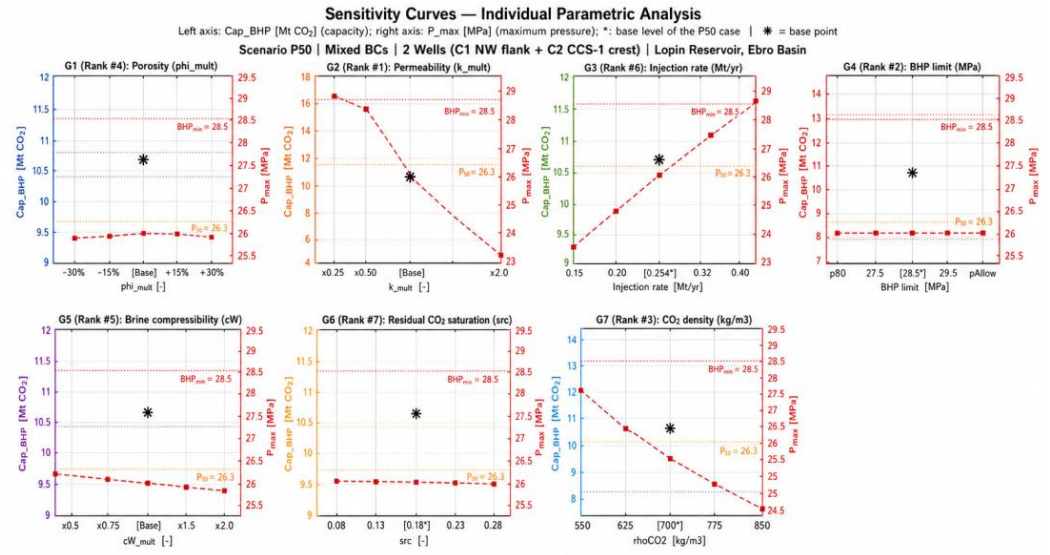


Figure 9. Individual sensitivity curves for the seven parameter groups evaluated. The dashed horizontal line represents the base-case capacity. The permeability, BHP limit, and CO_2 density curves show the strongest variations in Cap_BHP.

4.4. Secondary Control Mechanisms

Porosity has a limited effect on dynamic capacity. Although changing porosity modifies available pore volume, the capacity range remains narrow, between 10.34 and 10.76 Mt. This indicates that, under the evaluated conditions, pore volume is not the primary operational limitation.

Brine compressibility also produces a minor variation, with capacities between 10.59 and 10.92 Mt. This effect is consistent with the role of compressibility in pressure propagation, although its magnitude is much smaller than that of permeability or the BHP limit.

Injection rate does not modify the maximum capacity estimated by the BHP-search algorithm, which remains 10.76 Mt for all evaluated levels. This does not mean that injection rate is operationally irrelevant. Maximum pressure increases from 23.49 MPa at 0.15 Mt/year to 28.60 MPa at 0.40 Mt/year, placing the highest-rate case close to the operational BHP limit. Therefore, injection rate remains important for operational design, even if it does not change the final BHP-limited capacity calculated by the search algorithm.

To further relate flow rate and pressure response, an apparent injectivity proxy was calculated as $q/\Delta P$, where q is the total imposed injection rate and $\Delta P = P_{max} - P_{ref}$. This proxy is not intended to replace a well-test injectivity index, but it provides a consistent way to compare rate-induced pressure build-up within the VE model. The rate-sensitivity cases show that higher injection rates produce stronger pressure build-up, even though the final Cap_BHP remains unchanged under the adopted capacity-search formulation. Therefore, injection rate remains relevant for operational injectivity and pressure management, although it is not ranked as a controlling factor for Cap_BHP in this specific algorithm.

Residual CO_2 saturation also does not modify Cap_BHP over the evaluated range. Capacity remains constant at 10.760 Mt. This result reflects the fact that the capacity criterion is controlled by injection-period pressure, whereas residual saturation mainly affects post-injection redistribution and trapping.

4.5. Integrated Sensitivity Heatmap

The heatmap provides a compact comparison of the 35 sensitivity cases relative to the base case (Figure 10). The largest relative changes are concentrated in permeability, BHP

limit, and CO_2 density. Levels associated with porosity, brine compressibility, injection rate, and residual CO_2 saturation show small or negligible changes in dynamic capacity.

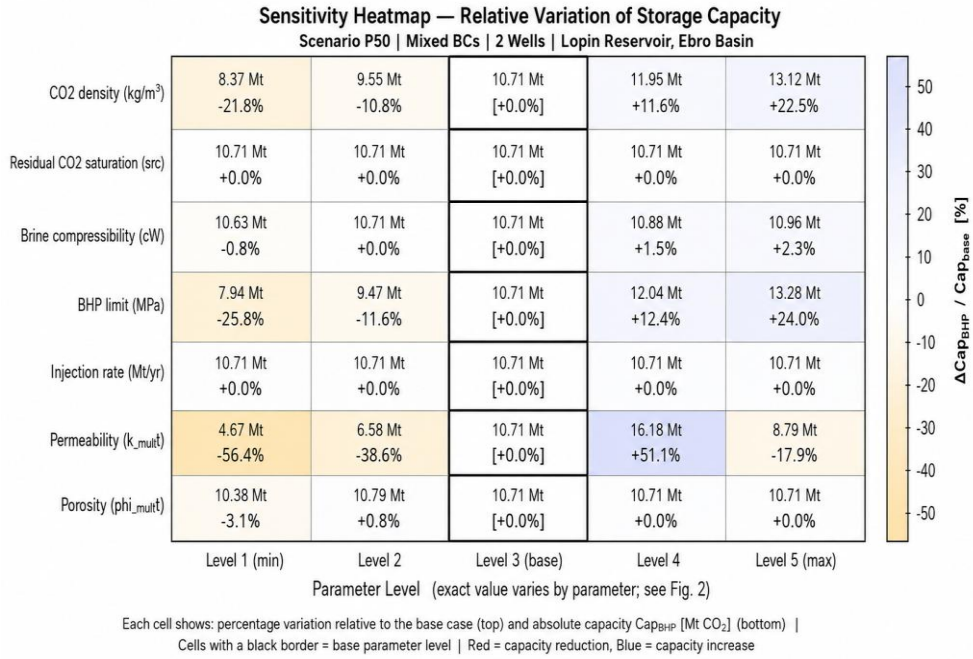


Figure 10. Heatmap of the sensitivity analysis. Each cell shows the relative variation in Cap_BHP compared with the base case and the absolute capacity value in Mt CO_2. The strongest changes are concentrated in permeability, BHP limit, and CO_2 density.

This visual synthesis reinforces the main result of the analysis: under the evaluated configuration, the operational capacity of the Lopín system is controlled primarily by the reservoir's ability to dissipate pressure rather than by static pore volume alone.

5. Discussion

5.1. Pressure-Limited Dynamic Capacity and Dominant Controls

The results show that CO_2 storage capacity in the Lopín structure cannot be interpreted solely as a function of available pore volume. Although porosity defines the physical space potentially available for CO_2 storage, its influence on pressure-limited dynamic capacity was secondary within the tested range. In contrast, horizontal permeability, the BHP limit, and CO_2 density explained most of the observed variability in maximum injectable mass.

This behavior supports the central hypothesis of the study: in fault-bounded saline aquifers, operational capacity depends primarily on the ability of the system to dissipate injection-induced overpressure. Therefore, the limiting factor is not simply how much CO_2 can be accommodated within the reservoir pore volume, but how much CO_2 can be injected without exceeding admissible pressure limits. This distinction is fundamental because static volumetric estimates may overestimate effective capacity when pressure evolution is not explicitly considered [3,5,12].

Horizontal permeability was the dominant parameter in the analysis. Its effect is explained by its control on reservoir transmissibility and, therefore, on the ability of the brine displaced by CO_2 injection to redistribute laterally [5,6]. Lower permeability promotes pressure build-up near the injection wells and reduces the maximum injectable mass. Conversely, higher permeability enhances pressure dissipation and increases capacity before the pressure limit is reached. In this sense, permeability is not only a petrophysical property of the reservoir, but also a direct control on the operational feasibility of storage.

The BHP limit appears as the second main control. In the base case, 28.5 MPa is used as an operational modeling threshold rather than as a fracture-pressure estimate. Its position below p90, pAllow, and pFrac preserves an explicit pressure buffer to the site-specific geomechanical limits reported for Lopín [30]. The sensitivity range from 26.31 to 30.50 MPa therefore quantifies how different conservative-to-permissive operational criteria affect the inferred dynamic capacity; it does not imply that all tested thresholds are equally acceptable for field operation. A final injection design would require site-specific coupled geomechanical analysis and validation of fault and seal stability. CO_2 density also has a significant influence because it modifies the relationship among injected mass, occupied volume, buoyancy, and pressure response.

5.2. Implications for Site Characterization and Pilot Design

The results have direct implications for early-stage geological CO_2 storage assessment. For systems like Lopín, the priority should not be limited to refining the available pore volume but should also focus on reducing uncertainty in the parameters that control pressure dissipation. Characterization of reservoir permeability and lateral transmissibility should be considered a priority, as these factors condition operational capacity under pressure constraints.

The definition of the BHP limit is also a critical design decision. A more conservative threshold reduces the estimated capacity, whereas a more permissive limit increases the maximum injectable mass. However, such an increase is acceptable only when supported by site-specific geomechanical evidence. In the present model, the 28.5 MPa base-case threshold provides a conservative buffer to the p90, pAllow, and pFrac values reported for Lopín [30]. BHP therefore functions as an operational link between hydraulic simulation and mechanical safety, but it does not replace coupled geomechanical assessment of reservoir deformation, fault stability, or induced-fracturing risk [6,10].

The influence of CO_2 density indicates that fluid properties must also be treated carefully. In this study, CO_2 density was represented by constant values selected to approximate dense-phase conditions at the Lopín reservoir depth, rather than by direct PVT measurements or a pressure-, temperature-, and salinity-dependent equation of state. This treatment is appropriate for the objective of the present study, which is to evaluate parametric controls on pressure-limited dynamic capacity under early-stage data availability, rather than to provide a full thermodynamic characterization of the storage complex. The reported density sensitivity therefore quantifies the effect of simplified fluid-property uncertainty on pressure-limited capacity and should not be interpreted as a complete thermodynamic assessment of CO_2 behavior under evolving reservoir conditions. Future work should incorporate site-specific temperature, salinity, and compositional data through an appropriate equation-of-state formulation.

5.3. Model Limitations

The VE approach enabled multiple sensitivity scenarios to be explored efficiently, but it has limitations that must be acknowledged. The formulation assumes that CO_2 segregates rapidly toward the top of the reservoir and that the main dynamics can be represented through vertically integrated columns [11,12]. This approximation is suitable for preliminary prospect-scale assessment, providing a more detailed level of analysis than regional-scale screening. However, it may not capture local-scale processes such as vertical channeling, subvertical heterogeneity, complex capillary effects, or migration through discrete fractures.

Faults are represented in a simplified way through structural traces and boundary conditions, but multiphase flow through fault planes and the evolution of fault perme-

ability are not explicitly modeled. This simplification is relevant because the hydraulic behavior of faults can modify pressure evolution, plume migration, and storage security. This uncertainty is particularly relevant because the main conclusion of this study depends on pressure dissipation and lateral transmissibility. If the bounding faults are more transmissive than assumed, pressure dissipation pathways and plume migration could differ from the present simulations. Conversely, if the east–west hydraulic connection with the regional aquifer is weaker than represented by the hydrostatic pressure boundaries, pressure build-up would be stronger and the estimated dynamic capacity would likely decrease. Therefore, the reported capacities should be interpreted as conditional on the adopted mixed-boundary representation.

Another important limitation is the absence of explicit geomechanical coupling. Pressure limits allow safety criteria to be incorporated, but they do not replace a complete analysis of reservoir deformation, fault stability, or induced-fracturing risk, and induced seismicity issues [6,10]. Therefore, the results should be interpreted as a preliminary dynamic flow-based assessment, not as a final demonstration of geomechanical safety. Because the OAT design varies one parameter at a time, interactions between permeability, porosity, fluid properties, boundary conditions, and operational criteria are not resolved. Future work should consider global sensitivity or uncertainty-propagation methods once a broader ensemble of geological and fluid-property realizations is available. Future work on Lopín should include coupled hydro-mechanical modeling to evaluate seal integrity and fault stability under injection-induced pressure changes.

Finally, the extreme permeability case $\times 4$ produced an anomalous numerical response with non-finite pressure. This result should not be interpreted as a robust physical response of the system, but as an indication of the numerical limits of the solver under conditions far from the base case. The main conclusion regarding the dominant role of permeability remains valid, but it should be supported by the overall behavior of the tested range rather than by this extreme point.

6. Conclusions

This research developed and applied a numerical VE workflow in MATLAB/MRST to evaluate the key parametric controls on dynamic CO_2 storage capacity in the Lopín structure, Ebro Basin, NE Spain. Unlike static volumetric estimates, the approach defines capacity as the maximum mass of CO_2 that can be injected over a 30-year period without exceeding an explicit operational BHP limit, thereby linking the capacity estimate to pressure-constrained injectability.

For the P50 reference configuration, plume evolution is controlled by the C1–C2 well layout, buoyancy-driven migration, structural relief, and lateral pressure dissipation through the open east–west boundaries. The long-term simulation shows that, after 1030 years, most of the CO_2 remains as a mobile phase, whereas residual, structural, and dissolution trapping provides additional immobilization.

The sensitivity analysis shows that dynamic capacity is controlled primarily by horizontal permeability, followed by the BHP limit and CO_2 density. Permeability produced the largest capacity variation, confirming that reservoir transmissibility and lateral pressure dissipation are critical factors for storage feasibility. In contrast, porosity, brine compressibility, nominal injection rate, and residual CO_2 saturation had a secondary influence within the tested ranges.

These findings support the central hypothesis of this work: in fault-bounded saline aquifers such as Lopín, operational capacity is not governed only by available pore volume, but by the hydraulic ability of the system to dissipate injection-induced overpressure. Early-stage geological CO_2 storage assessments should therefore prioritize permeabil-

ity characterization, lateral connectivity, transparent justification of operational pressure thresholds, and accurate representation of CO_2 thermodynamic properties. For Lopín, coupled geomechanical assessment and improved characterization of fault transmissibility remain essential before the sensitivity-based pressure limits can be translated into field-operational criteria.

Author Contributions: Conceptualization, C.A.Q.-T.; methodology, C.A.Q.-T.; software, C.A.Q.-T.; validation, C.A.Q.-T.; formal analysis, C.A.Q.-T.; investigation, C.A.Q.-T.; resources, J.G.-C. and P.F.-C.; data curation, C.A.Q.-T.; writing—original draft preparation, C.A.Q.-T.; writing—review and editing, C.A.Q.-T., M.G.-O., I.H., J.G.-C. and P.F.-C.; visualization, C.A.Q.-T.; supervision, M.G.-O. and I.H.; project administration, I.H. All authors have read and agreed to the published version of the manuscript.

Funding: This research was funded by the Institut Cartogràfic i Geològic de Catalunya (ICGC) through a student grant awarded to the first author, C.A.Q.T, within the Master's Degree in Renewable Energy and Energy Sustainability, Faculty of Physics, University of Barcelona (UB), 08028 Barcelona, Spain.

Data Availability Statement: The geological and petrophysical input data were provided by IGME-CSIC within the European H2020 PilotSTRATEGY project (Grant Agreement No. 101022664), and are subject to the access conditions of the data owners and project partners. Requests for access to the source data should be directed to the relevant data owners. Derived numerical outputs may be made available by the corresponding author upon reasonable request, subject to those restrictions.

Acknowledgments: The authors thank IGME-CSIC and the PilotSTRATEGY consortium for providing geological and petrophysical data, and the ICGC and UB for institutional and scientific support during the development of the modeling work. We acknowledge support from grants PID2022-140850OB-C21 and PID2022-140850OB-C22 from MICIU/AEI/10.13039/501100011033 and 'ERDF/EU' and the "Consolidación Investigadora" grant CNS2023-145382 funded by MCIN/AEI/10.13039/50110001103. Additional support was provided by the Generalitat de Catalunya (2021SGR00076). During the preparation of this manuscript, the authors used generative artificial intelligence tools, including Gemini (versions 3.1 Pro and 3.6 Flash) and Claude (Sonnet 5), solely for translation and editorial support, such as restructuring paragraphs and improving the organization and readability of the text. These tools were not used to generate scientific content, develop the methodology, analyze or interpret data, produce results or conclusions, or otherwise influence the originality, intellectual contribution, or scientific merit of the manuscript. The authors reviewed and edited all AI-assisted output and take full responsibility for the content of this publication.

Conflicts of Interest: The authors declare no conflicts of interest.

Abbreviations

The following abbreviations are used in this manuscript:

MRST	MATLAB Reservoir Simulation Toolbox
VE	Vertical Equilibrium
BHP	Bottom-Hole Pressure
CCS	Carbon Capture and Storage
CapBHP	Pressure-Limited Dynamic Capacity

References

1. IPCC. *IPCC Special Report on Carbon Dioxide Capture and Storage*; Metz, B., Davidson, O., de Coninck, H., Loos, M., Meyer, L., Eds.; Cambridge University Press: Cambridge, UK, 2005.
2. IEA. *Carbon Capture, Utilisation and Storage*; International Energy Agency: Paris, France, 2023; IEA Website. Available online: https://www.iea.org/energy-system/renewables-and-low-emissions/carbon-capture-utilisation-and-storage (accessed on 10 July 2026).

3. Worden, R.H. Carbon Dioxide Capture and Storage (CCS) in Saline Aquifers versus Depleted Gas Fields. *Geosciences* **2024**, *14*, 146. [CrossRef]
4. Massarweh, O.; Abushaikha, A.S. CO_2 sequestration in subsurface geological formations: A review of trapping mechanisms and monitoring techniques. *Earth-Sci. Rev.* **2024**, *253*, 104793. [CrossRef]
5. Bachu, S. Review of CO_2 storage efficiency in deep saline aquifers. *Int. J. Greenh. Gas. Control* **2015**, *40*, 188–202. [CrossRef]
6. Zhou, Q.; Birkholzer, J.T.; Tsang, C.-F.; Rutqvist, J. A method for quick assessment of CO_2 storage capacity in closed and semi-closed saline formations. *Int. J. Greenh. Gas. Control* **2008**, *2*, 626–639. [CrossRef]
7. Birkholzer, J.T.; Oldenburg, C.M.; Zhou, Q. CO_2 migration and pressure evolution in deep saline aquifers. *Int. J. Greenh. Gas. Control* **2015**, *40*, 203–220. [CrossRef]
8. Szulczewski, M.L.; MacMinn, C.W.; Juanes, R. Theoretical analysis of how pressure buildup and CO_2 migration can both constrain storage capacity in deep saline aquifers. *Int. J. Greenh. Gas. Control* **2014**, *23*, 113–118. [CrossRef]
9. Thibeau, S.; Mucha, V. Have we overestimated saline aquifer CO_2 storage capacities? *Oil Gas. Sci. Technol.* **2011**, *66*, 81–92. [CrossRef]
10. Rutqvist, J. The geomechanics of CO_2 storage in deep sedimentary formations. *Geotech. Geol. Eng.* **2012**, *30*, 525–551. [CrossRef]
11. Nordbotten, J.M.; Celia, M.A. Similarity solutions for fluid injection into confined aquifers. *J. Fluid Mech.* **2006**, *561*, 307–327. [CrossRef]
12. Nilsen, H.M.; Lie, K.-A.; Andersen, O. Robust simulation of sharp-interface models for fast estimation of CO_2 trapping capacity in large-scale aquifer systems. *Comput. Geosci.* **2016**, *20*, 93–113. [CrossRef]
13. Lie, K.-A. *An Introduction to Reservoir Simulation Using MATLAB/GNU Octave: User Guide for the MATLAB Reservoir Simulation Toolbox (MRST)*; Cambridge University Press: Cambridge, UK, 2019.
14. Lie, K.-A.; Nilsen, H.M.; Andersen, O.; Møyner, O. A simulation workflow for large-scale CO_2 storage in the Norwegian North Sea. *Comput. Geosci.* **2016**, *20*, 607–622. [CrossRef]
15. Nilsen, H.M.; Lie, K.-A.; Møyner, O.; Andersen, O. Spill-point analysis and structural trapping capacity in saline aquifers using MRST-co2lab. *Comput. Geosci.* **2015**, *75*, 33–43. [CrossRef]
16. Nilsen, H.M.; Lie, K.-A.; Andersen, O. Analysis of CO_2 trapping capacities and long-term migration for geological formations in the Norwegian North Sea using MRST-co2lab. *Comput. Geosci.* **2015**, *79*, 15–26. [CrossRef]
17. Andersen, O.; Lie, K.-A.; Nilsen, H.M. An open-source toolchain for simulation and optimization of aquifer-wide CO_2 storage. *Energy Procedia* **2016**, *86*, 324–333. [CrossRef]
18. Møyner, O.; Nilsen, H.M. Multiresolution coupled vertical equilibrium model for fast flexible simulation of CO_2 storage. *Comput. Geosci.* **2019**, *23*, 1–20. [CrossRef]
19. Saló-Salgado, L.; Møyner, O.; Lie, K.-A.; Juanes, R. Three-dimensional simulation of geologic carbon dioxide sequestration using MRST. *Adv. Geo-Energy Res.* **2024**, *14*, 34–48. [CrossRef]
20. de Jonge-Anderson, I.; Ramachandran, H.; Nicholson, U.; Geiger, S.; Widyanita, A.; Doster, F. Determining CO_2 storage efficiency within a saline aquifer using reduced complexity models. *Adv. Geo-Energy Res.* **2024**, *13*, 22–31. [CrossRef]
21. Temizel, C.; Karcıoğlu, G.; Behzadan, A.; Çetin, C.; Pamukçu, Y.Z. A Comparative Study of Solvers and Preconditioners for an SPE CO_2 Storage Benchmark Reservoir Simulation Model. *Geosciences* **2025**, *15*, 169. [CrossRef]
22. Zeynolabedini, M.; Jahanbani Ghahfarokhi, A. Vertical Equilibrium Model Analysis for CO_2 Storage. *Gases* **2025**, *5*, 16. [CrossRef]
23. Alcalde, J.; Marzán, I.; Saura, E.; Martí, D.; Ayarza, P.; Juhlin, C.; Pérez-Estaún, A.; Carbonell, R. 3D geological characterization of the Hontomín CO_2 storage site, Spain: Multidisciplinary approach from seismic, well-log and regional data. *Tectonophysics* **2014**, *627*, 6–25. [CrossRef]
24. de Dios, J.C.; Delgado, M.A.; Martínez, C.; Ramos, A.; Álvarez, I.; Marín, J.A.; Salvador, I. Hydraulic characterization of fractured carbonates for CO_2 geological storage: Experiences and lessons learned in Hontomín Technology Development Plant. *Int. J. Greenh. Gas. Control* **2017**, *58*, 185–200. [CrossRef]
25. Le Gallo, Y.; de Dios, J.C.; Salvador, I.; Acosta Carballo, T. Geological Model of a Storage Complex for a CO_2 Storage Operation in a Naturally-Fractured Carbonate Formation. *Geosciences* **2018**, *8*, 354. [CrossRef]
26. Mateos-Redondo, F.; Kovács, T.; Berrezueta, E. Petrographic and Petrophysical Characterization of Detrital Reservoir Rocks for CO_2 Geological Storage (Utrillas and Escucha Sandstones, Northern Spain). *Geosciences* **2018**, *8*, 246. [CrossRef]
27. Ordóñez, B.; Mediato, J.F.; Kovács, T.; Martínez-Martínez, J.; Fernández-Canteli, P.; González-Menéndez, L.; Roces, S.; Caicedo-Potosí, J.; del Moral, B.; Berrezueta, E. Experimental geochemical assessment of a seal-reservoir system exposed to supercritical CO_2: A case study from the Ebro Basin, Spain. *Int. J. Greenh. Gas. Control* **2024**, *137*, 104233. [CrossRef]
28. Ayala, C.; Benjumea, B.; Mediato, J.F.; García-Crespo, J.; Clariana, P.; Soto, R.; Rubio, F.; Rey-Moral, C.; Pueyo, E.L.; Martín-León, J.; et al. Developing a new innovative methodology to integrate geophysical techniques into characterization of potential CO_2 storage sites: Lopín structure, southern Ebro Basin, Spain. *Geol. Soc.* **2023**, *528*, 227–243. [CrossRef]

29. Wilkinson, M. Conceptual Geological Models of Portugal, Spain and France; PilotSTRATEGY Project, Deliverable D2.7; Horizon 2020 Grant Agreement No. 101022664, 2023. Available online: https://pilotstrategy.eu/sites/default/files/2023-08/D2.7_ConceptualGeolModels.pdf (accessed on 10 July 2026).
30. Eguilior, S.; Hurtado, A.; Recreo, F. Recommendations for Safety and Performance Analyses of Storage Pilot in the Ebro Basin; PilotSTRATEGY Project, Deliverable D5.3; Horizon 2020 Grant Agreement No. 101022664. 2025. Available online: https://pilotstrategy.eu/sites/default/files/2026-01/PilotSTRATEGY_D5.3_Safety%20and%20performance%20analysis%20Ebro%20Basin.pdf (accessed on 10 July 2026).
31. Instituto Geológico y Minero de España (IGME). Geological Storage of CO_2 Plan (ALGECO2 Project). Spanish Geological Survey (IGME): Madrid, Spain. 2010. Available online: https://info.igme.es/algeco2/ (accessed on 10 July 2026).
32. Geological Service for Europe (GSEU) Project. Online Pan-European Atlas of Sustainable Geo-Energy Capacities. European Geological Data Infrastructure (EGDI): Brussels, Belgium. 09 September 2026. Available online: https://maps.europe-geology.eu/ (accessed on 20 September 2026).
33. Gil-Ortiz, M.; Gomez-Rivas, E.; Alcalde, J.; Cabello, P.; Yeste, L.M.; Zamora, G.; Carrasco, Á.; García Fernández-Valderrama, D.; Martín-Monge, A.; Mañas, M.; et al. Characterization of the Miocene Castellón Sandstones Formation in the Western Mediterranean as a potential geological carbon storage site. *Mar. Pet. Geol.* **2025**, *181*, 107493. [CrossRef]
34. Martín Monge, A.; Mañas Fernández, M.; Olgado Azpiazu, V.; Torres Torremocha, J.; Vayssaire, A.; Pángaro, F. Sealing potential of the Ebro Formation, offshore Ebro Basin: Implications for the safe storage of CO_2. In Proceedings of the 86th EAGE Annual Conference, Toulouse, France, 2 June 2025; European Association of Geoscientists & Engineers: Bunnik, The Netherlands, 2026; Volume 2025, pp. 1–5. [CrossRef]
35. STRATEGY CCUS Project. Strategic Planning of Regions and Territories in Europe for Low-Carbon Energy and Industry Through CCUS; Horizon 2020 Project, Grant Agreement No. 837754, 2019–2022. Available online: https://www.igme.es/en/proyecto/strategy-ccus-project/ (accessed on 10 July 2026).

Disclaimer/Publisher's Note: The statements, opinions and data contained in all publications are solely those of the individual author(s) and contributor(s) and not of MDPI and/or the editor(s). MDPI and/or the editor(s) disclaim responsibility for any injury to people or property resulting from any ideas, methods, instructions or products referred to in the content.